



CHALMERS
UNIVERSITY OF TECHNOLOGY

**High energy density and reliable
 $\text{BaZr}_x\text{Ti}_{1-x}\text{O}_3$ thin film capacitors from**

Downloaded from: <https://research.chalmers.se>, 2025-05-31 23:19 UTC

Citation for the original published paper (version of record):

Angermann, M., Panzic, I., Kobald, A. et al (2025). High energy density and reliable $\text{BaZr}_x\text{Ti}_{1-x}\text{O}_3$ thin film capacitors from novel aqueous chemical solution deposition. *Journal of the European Ceramic Society*, 45(12). <http://dx.doi.org/10.1016/j.jeurceramsoc.2025.117465>

N.B. When citing this work, cite the original published paper.



High energy density and reliable $\text{BaZr}_x\text{Ti}_{1-x}\text{O}_3$ thin film capacitors from novel aqueous chemical solution deposition

Martina Angermann^{a,*} , Ivana Panzic^a, Alexander M. Kobald^a, Herbert Kobald^a ,
Theresa Gindel^a, Kristine Bakken^b , Marco Deluca^{c,*} 

^a Materials Center Leoben Forschung GmbH, Department of Microelectronics, Kerpelystrasse 2, Leoben 8700, Austria

^b Chalmers University of Technology, Department of Physics, Kemigården 1, Göteborg 412 96, Sweden

^c Silicon Austria Labs GmbH, Sandgasse 34, Graz 8010, Austria

ARTICLE INFO

Keywords:

BZT
Aqueous chemical solution deposition
Dielectric properties
Relaxors

ABSTRACT

High energy density capacitors are essential in portable energy-autonomous devices for the Internet of Things (IoT). Capacitors based on perovskite ferroelectric thin films, where substitution breaks down ferroelectricity to the local scale, are interesting due to their improved energy density, efficiency and breakdown strength. For this work, Mn-substituted (1.5 %) Barium Zirconate Titanate ($\text{BaZr}_x\text{Ti}_{1-x}\text{O}_3$, BZT) thin films were prepared on Pt/Si substrates via a novel aqueous chemical solution deposition (CSD) process using entirely environmentally friendly chemicals. The thin films were investigated with Grazing incidence X-ray Diffraction (GI-XRD), Raman Spectroscopy, Scanning Electron Microscopy (SEM), Atomic Force Microscopy (AFM) and dielectric/ferroelectric characterization under application-relevant conditions. All thin films exhibit a highly crystalline and dense microstructure with a smooth surface. All compositions offer high energy density and efficiency, whereby the best results were obtained at 15 % Zr content, with a high recoverable energy density (11 Jcm^{-3} at 1.8 MVcm^{-1}), high fatigue resistance, high frequency and temperature stability with deviations from the reference state (lowest value) of less than 3 % (10^6 cycles), 5 % (0.1–100 kHz) and 16 % (20–200°C), respectively. These thin films are highly suitable as capacitors for IoT devices, and moreover, they are prepared using a green process.

1. Introduction

Ferroelectric materials are highly desirable for capacitive energy storage applications due to their rapid charge-discharge mechanisms and high-power densities [1–3]. However, ferroelectric materials typically suffer from significant hysteretic losses, attributed to their high remnant polarization in comparison to their saturation polarization. In contrast, ‘relaxors’, typically exhibit slimmer polarization hysteresis loops corresponding to lower losses, rendering them more suitable for energy storage applications. The relaxor behavior in perovskites is typically induced through chemical modification, where substituted cations disrupt long-range ferroelectric order down to the nanoscale [4]. As such, relaxor perovskites combine both a slim polarization hysteresis loop and a high dielectric breakdown strength, in general achieving superior recoverable energy densities compared to the ferroelectric counterparts. They are, thus, interesting as energy buffer materials for portable energy autonomous devices, e.g. for the Internet of Things (IoT).

$\text{BaZr}_x\text{Ti}_{1-x}\text{O}_3$ (BZT) is one of the most studied ferroelectric solid solutions where substitution induces a transition towards relaxor behavior [5–8]. In BZT bulk ceramics, within the range $x = 0$ –0.25 the ferroelectric state occurs, while at higher Zr content the relaxor state is present [9]. Most studies suggest that, in bulk ceramics, the crossover region lies between $x = 0.2$ –0.3, where optimal energy storage properties are anticipated, coinciding with the onset of relaxor behavior [6,10,11]. Compositions in the crossover region typically display high dielectric constants, reduced remnant polarization, temperature stability and fatigue resistance, due to a maximum reorientation capability of the short-range polar order [12]. In thin films, the crossover region is typically found at lower Zr content compared to bulk ceramics, likely due to their smaller grain sizes [13]. Hence, the Zr amount needs to be carefully tested and optimized for different preparation techniques.

For device miniaturization, thin films are preferable as the microstructure can be tailored and the reorientation of polar domains is enhanced by texture, resulting in higher maximum energy density and increased energy storage efficiency. Moreover, dielectric breakdown

* Corresponding authors.

E-mail addresses: martina.angermann@mcl.at (M. Angermann), marco.deluca@silicon-austria.com (M. Deluca).

<https://doi.org/10.1016/j.jeurceramsoc.2025.117465>

Received 3 October 2024; Received in revised form 29 March 2025; Accepted 14 April 2025

Available online 14 April 2025

0955-2219/© 2025 The Authors. Published by Elsevier Ltd. This is an open access article under the CC BY license (<http://creativecommons.org/licenses/by/4.0/>).

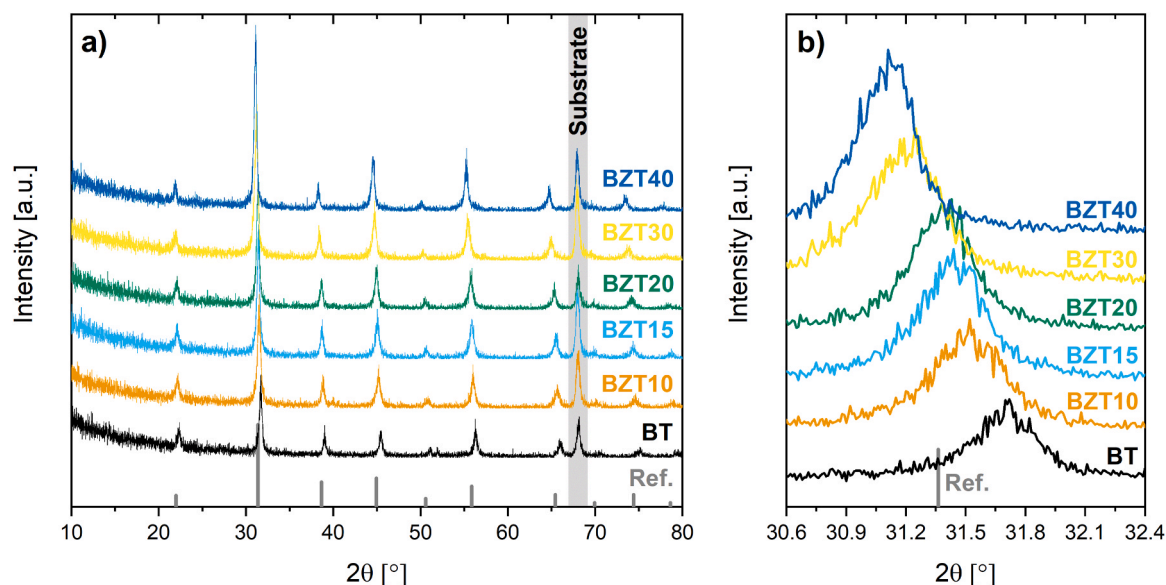


Fig. 1. (a) GIXRD patterns of the BZT thin films and a reference (bottom) cubic BaTiO_3 (ICDD PDF#31-0174); (b) The {110} peak shift demonstrating the incorporation of Zr on the perovskite B-site.

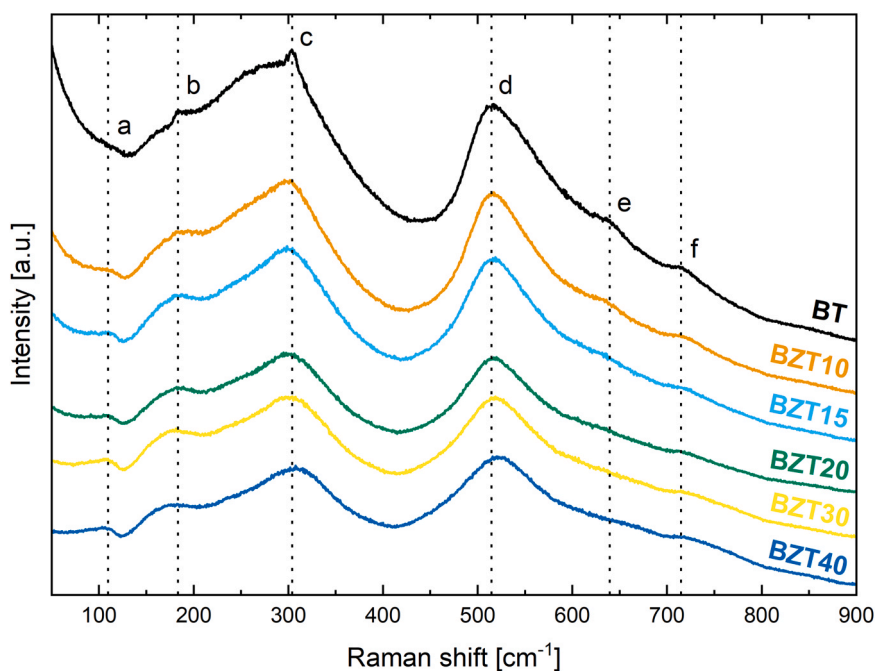


Fig. 2. Normalized Raman spectra of BT, BZT10, BZT15, BZT20, BZT30 and BZT40 thin films at room temperature. The lines a-f mark the characteristic peaks of the BZT Raman spectra.

strengths are typically higher in thin films due to a decreased likelihood of critical structural defects [14,15]. Achieving high-quality thin films is only possible with a reliable fabrication procedure enabling precise control over chemistry and properties. Chemical solution deposition (CSD) is a suitable, cost-effective, and flexible method for industrial-scale production of oxide thin films. However, the majority of literature focuses on organic synthesis routes, which use highly-toxic solvents such as 2-methoxyethanol. Although aqueous solutions would be suitable for CSD and a more environmentally friendly alternative, they have received little attention for the production of perovskite thin films so far.

Barium Titanate (BT) based thin films prepared via CSD are typically prone to high leakage currents, which affect the electrical output of

capacitors, especially with increasing temperature and electric fields [16]. This is also true for BT thin films from aqueous CSD, but epitaxy and texture has been shown to improve the electrical properties in BT and $(\text{Ba,Ca})(\text{Zr,Ti})\text{O}_3$ films, depending on the substrate used [17,18]. Despite the advantages of aqueous CSD, the work on BZT thin films is limited to that of Hardy *et al.*, which did not include any electrical characterization [19]. One strategy for mitigating leakage currents in BT-based thin films is B-site substitution with Mn, which is expected to be beneficial to the electrical performance, since Mn can adopt multiple oxidation states and thus can decrease the concentration of oxygen vacancies and electrons stemming from high-temperature consolidation processes [20].

In this paper, we present a novel and flexible aqueous CSD procedure

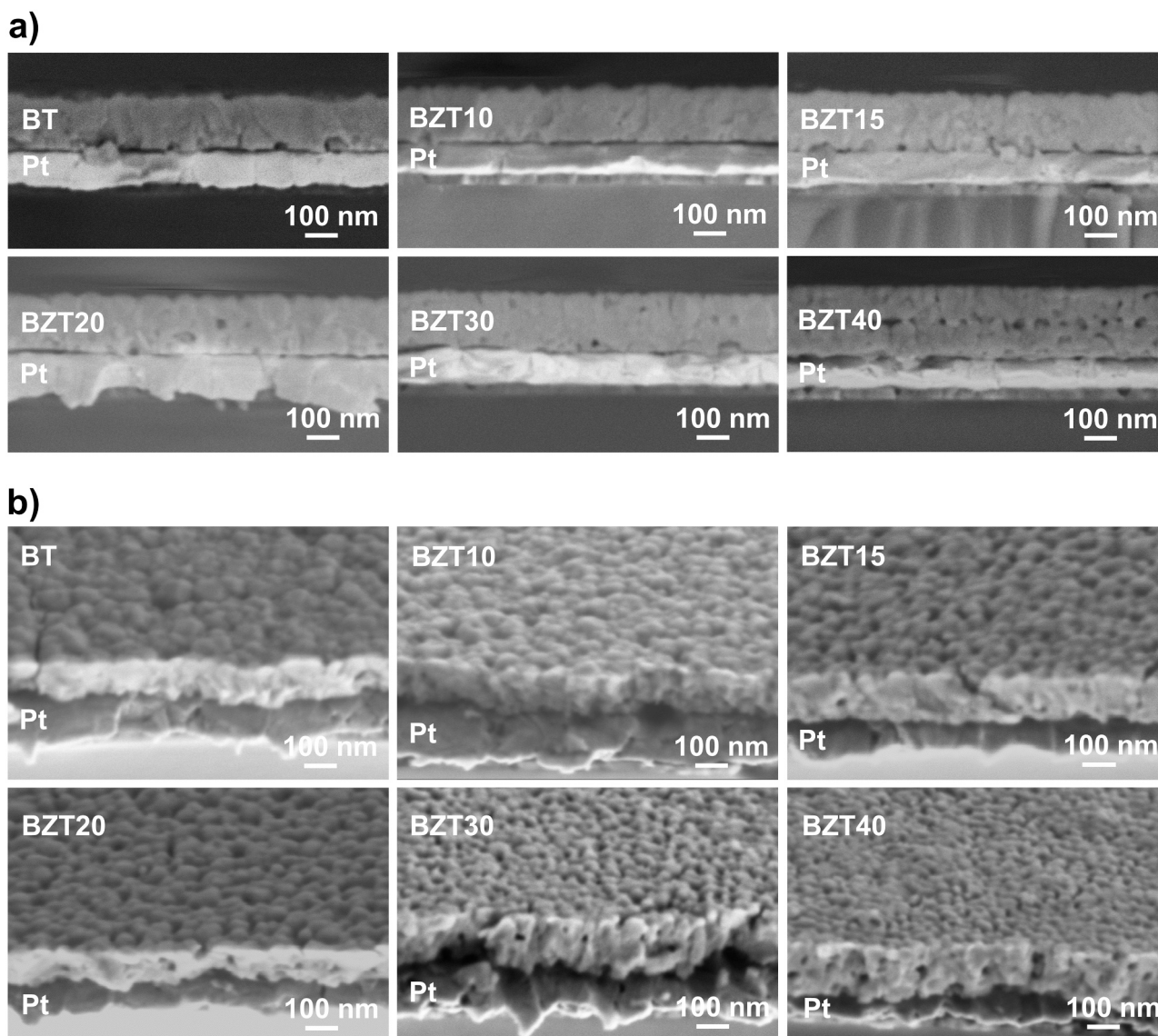


Fig. 3. SEM images of BT, BZT10, BZT15, BZT20, BZT30 and BZT40 thin films on the 100 nm thick Pt substrate. The samples were broken, and hence pulled out Pt and rough edges are visible. (a) Cross-section, (b) tilted view (30°) showing the surface and cross-section.

for producing BZT thin films. The produced thin films were fully characterized regarding their microstructure (SEM, AFM), phase-purity (GI-XRD, Raman spectroscopy) and electrical properties, highlighting their excellent energy storage performance and long-term stability. Dense and phase pure perovskite thin films on Pt/Si substrates were produced with Mn-substitution (1.5 % on the B-site), which helped to eliminate leakage currents for a range of BZT compositions ($x = 0-0.40$). This work demonstrates that high-quality and reliable relaxor-like BZT thin films can be produced from aqueous CSD, whereby the use of water-based precursor solutions offers an economic, environmentally-friendly and safe alternative to organic precursor solutions using toxic chemicals. Lastly, important aspects of optimizing the thin film fabrication parameters and composition are outlined in regard to high energy density and reliability for energy storage applications.

2. Material and methods

2.1. Solution preparation

The preparation of the Mn-substituted BZT thin films was done by adaptation of the synthesis routes reported in previous work on BT based

thin films [17,18,21]. Precursor solutions with nominal stoichiometry corresponding to $\text{Ba}(\text{Zr}_x\text{Ti}_{1-x})_{0.985}\text{Mn}_{0.015}\text{O}_3$ solutions with $x = 0, 0.10, 0.15, 0.20, 0.30, 0.40$ were prepared by mixing separate aqueous Ba-, Zr-, Ti- and Mn-complex solutions. All BZT solutions were diluted to 0.075 M and mixed according to the required Zr content, which we refer to in our notation (BZTx, where x is in percent). Additionally, 'pure' BT solution (0.075 M $\text{BaTi}_{0.985}\text{Mn}_{0.015}\text{O}_3$) was prepared.

The aqueous Ba-solution was prepared with a molar ratio of 1:2:1 (Ba $(\text{NO}_3)_2$:citric acid:EDTA, respectively): Prior to mixing, $\text{Ba}(\text{NO}_3)_2$ (Roth, Germany) was dried overnight at 200°C and then added to a pre-made aqueous solution of EDTA (Sigma-Aldrich, USA) and ammonia solution (Sigma-Aldrich, USA). Afterwards, citric acid was dissolved in the mixture, before the pH was adjusted to neutral by the addition of ammonia solution. The Ti-solution had a molar ratio of 1:3 (Ti:citric acid, respectively) and was prepared by stirring $\text{Ti}[\text{OCH}(\text{CH}_3)_2]_4$ (Sigma-Aldrich, USA) in an aqueous solution of citric acid overnight at 80°C, before adjusting the pH to neutral by the addition of ammonia solution. The Zr-solution with a molar ratio of 1:2 (Zr:citric acid, respectively) was prepared by dissolving $\text{Zr}(\text{NO})(\text{NO}_3)_2 \cdot 6\text{H}_2\text{O}$ (Sigma Aldrich, USA) in an aqueous solution of citric acid. The Mn-solution was prepared by dissolving $\text{Mn}(\text{CH}_3\text{COO})_2 \cdot 4\text{H}_2\text{O}$ (Sigma Aldrich, USA) in

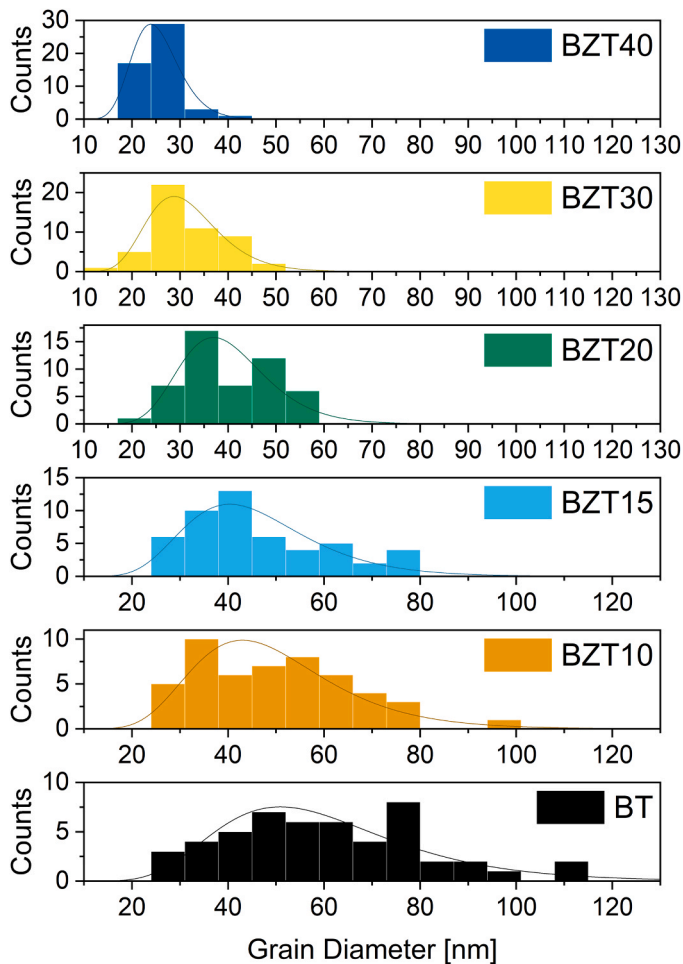


Fig. 4. Lognormal distributions and histograms of the grain diameters of BT, BZT10, BZT15, BZT20, BZT30 and BZT40 thin films, derived from the SEM images by measuring the width of 50 grains per image.

water.

2.2. Thin film preparation

$1 \times 1 \text{ cm}^2$ sized Pt/Si substrates (100 nm Pt/20 nm TiO_2 /600 nm SiO_2 /Si, SINTEF, Norway), were plasma-cleaned by O_2 -plasma prior to deposition of the BZT precursor solutions by spin coating (SPIN150i, APT GmbH, Germany) at 3000 rpm (500 rpm^{-1}) for 30 s, followed by a drying step on a hotplate for 2 min at 100°C . The films were then heated in a rapid thermal annealer (RTA) furnace (MILA-5050, ULVAC GmbH, Germany) first to 450°C (1°Cs^{-1} , 1 min hold) and then crystallized at 850°C (10°Cs^{-1} , 5 min hold) in synthetic air (80 % N_2 and 20 % O_2) in the same RTA furnace. The last layer was held at 850°C for 30 min instead of 5 min to improve the crystallinity of the films. The heating program was designed to limit the effects of possible intermediate phases on the final microstructure of the films [18]. The deposition cycle was repeated 19 times to yield a final film thickness of $\sim 150 \text{ nm}$.

2.3. Characterization

The crystal structure and phase purity of the thin films were investigated by Grazing Incidence X-ray diffraction (GI-XRD) on a Bruker D8 Advance (Karlsruhe, Germany) diffractometer using $\text{CuK}\alpha$ irradiation at 40 kV accelerating voltage and 25 mA current. Samples were measured in continuous mode with a 2θ -angle ranging from 10° to 80° with 0.01° steps, a scan rate of 2° min^{-1} and an incidence angle of 0.80° . Raman

measurements were performed with a WITec alpha300R spectrometer (WITec GmbH, Ulm, Germany) with an 1800 gr/mm grating and an 100x EC Epiplan-Neofluar DIC objective (Zeiss, Germany) using a 532 nm laser as excitation source with a nominal power of 10 mW. The thin film morphology and the thickness of the cleaved cross-sections were investigated with scanning electron microscopy (SEM) in an Auriga 40 instrument (Zeiss, Germany). The thicknesses of the thin films were determined from the SEM-images by averaging 10 values of measured thickness. Atomic Force Microscopy (AFM) characterization was performed using CoreAFM (Nanosurf, Switzerland) under ambient conditions. Non-contact (tapping) mode was used for image acquisition. The Tap300AI-G probe with a nominal resonance frequency of 300 kHz and a tip radius of less than 10 nm proved to be the best solution for this characterization. The scan parameters were initialized with a value of 15 % of nominal force and an acquisition time of 0.78 s on an area of $10 \times 10 \mu\text{m}$. Images were processed using the Gwyddion program [22].

Au/Cr top electrodes and contact pads to the Pt bottom electrode for electrical measurements were deposited via e-beam assisted evaporation (HEX Series TAU, Korvus Technology, United Kingdom) using a shadow mask with an electrode diameter of 1 mm and a large contact pad area ($4.8 \text{ mm} \times 1.3 \text{ mm}$), respectively. This way, for each $1 \times 1 \text{ cm}^2$ specimen, up to 12 metal-insulator-metal (MIM) capacitor structures were built, which were used for the electrical characterization. The electrical measurements were performed with an aixACCT TF3000 analyzer (aixACCT, Germany) using tungsten needles with a tip radius of $20 \mu\text{m}$. The measurements were either performed by contacting two top electrodes (dot2dot) or by contacting one top electrode with the bottom electrode (bottom2dot).

The recoverable energy density (W_{rec}) was calculated using the following integral function [23]:

$$W_{\text{rec}} = \int_{P_r}^{P_{\text{max}}} E dP, \quad (1)$$

where E is the electric field, P_{max} is the maximum polarization, and P_r is the remnant polarization. The area enclosed in the hysteretic loop represents the energy loss (W_{loss}), caused by elastic energy dissipation upon domain switching. Hence, the efficiency (η) of the switching process can be derived using the following formula:

$$\eta = \frac{W_{\text{rec}}}{W_{\text{rec}} + W_{\text{loss}}} \quad (2)$$

The tunability (T) was calculated using the relative permittivity (ϵ_r), according to this equation:

$$T = \frac{\epsilon_{r,\text{max}} - \epsilon_r}{\epsilon_{r,\text{max}}} \quad (3)$$

3. Results and discussion

3.1. Structural characterization

The GI-XRD diffraction patterns of the BZT thin film series are shown (Fig. 1), along with a cubic BaTiO_3 reference (ICDD PDF#31-0174). The thin films consist of a single highly crystalline perovskite phase, since the sharp peaks are consistent with the reference and no secondary peaks were detected, apart from those attributed to the substrate (the peak around $2\theta=68^\circ$ was assigned to Pt). No significant peak splitting was observed, but only a slight peak broadening at $2\theta=38.8^\circ$ for BZT15 and BZT20, which indicates a tetragonal structure. It is well known that a mix of cubic and tetragonal perovskite phase is often present in nanocrystalline BT and BZT material systems [24].

The diffraction patterns show that all peaks exhibit a shift to lower 2θ -values with increasing Zr amount in the thin films. This shift is most noticeable for the $\{110\}$ peak (Fig. 1b), and demonstrates the successful incorporation of Zr into the perovskite crystal lattice on the B-site [25]. The expansion of the lattice (peak shift to lower 2θ -values) with

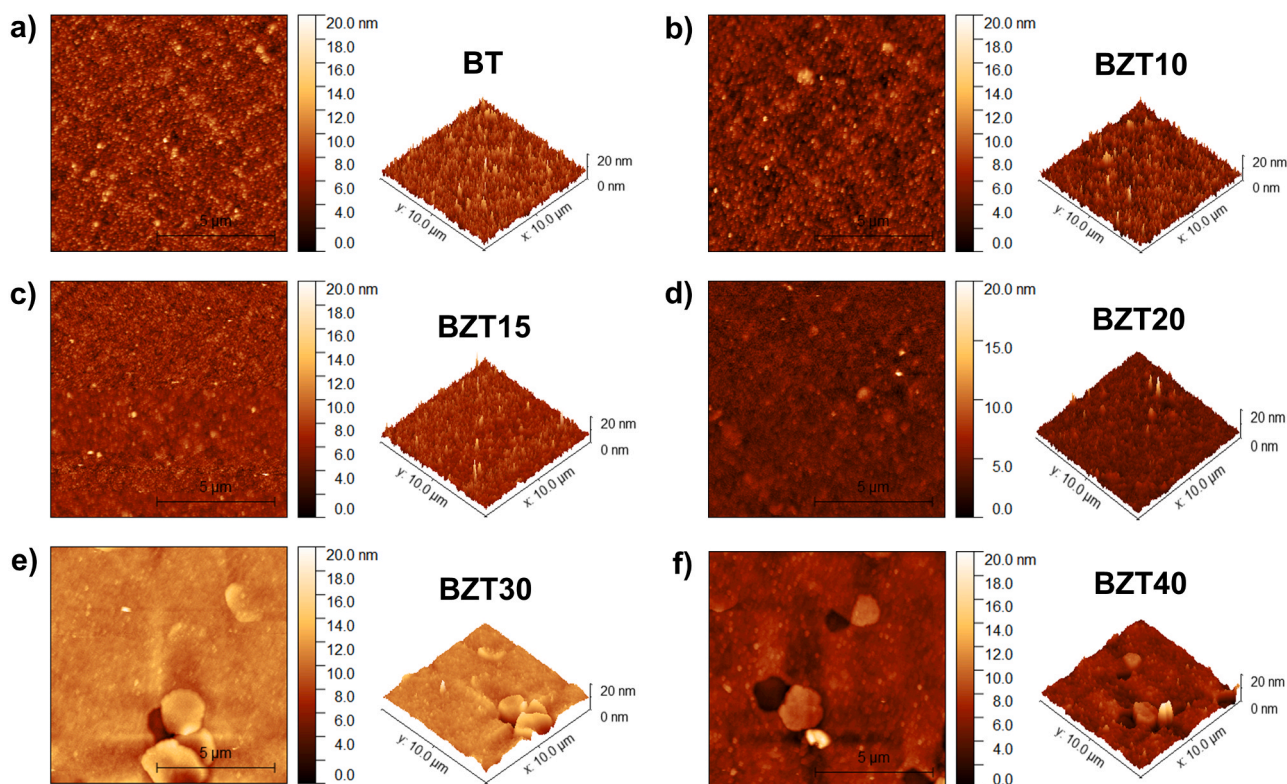


Fig. 5. AFM micrographs of (a) BT, (b) BZT10, (c) BZT15, (d) BZT20, (e) BZT30 and (f) BZT40 thin films; on the left side of each image is the top view, on the right side the 3D topography.

Table 1
Roughness parameters for all samples.

Sample	S_a	S_q
BT	2.59 nm	3.36 nm
BZT10	1.90 nm	2.48 nm
BZT15	2.75 nm	3.67 nm
BZT20	3.06 nm	4.12 nm
BZT30	5.22 nm	8.00 nm
BZT40	6.72 nm	9.83 nm

increasing Zr content is expected, since the ionic radius of Zr^{4+} is larger than that of Ti^{4+} (0.72 Å compared to 0.60 Å)[26]. Contrary to initial expectations that Zr might enhance tetragonality, the evolution of the diffraction patterns suggests that increasing Zr content stabilizes the cubic phase, as evidenced by the reduction of tetragonal peak splitting and the merging of the (200)/(002) reflections. The systematic increase in relative intensity of the {110} peak does not necessarily indicate improved crystallization or a stronger preferred orientation but is rather a consequence of the microstructural transition from a columnar to a more randomly oriented polycrystalline structure. This aligns with the observed suppression of the $\langle 100 \rangle$ texture upon Zr addition, as GIXRD data suggest a diminished degree of preferential orientation. Thus, the shift from columnar to polycrystalline morphology, along with the observed XRD trends, is consistent with a transition toward a more isotropic grain orientation.

Raman spectra of the BZT films (including BT) were taken at room temperature as shown in Fig. 2. The Raman spectra of BT resembles that of the tetragonal structure, indicated by the peaks *b*, *c*, *d*, *f* in the figure, which correspond to the following modes: E(TO+LO) and A1(LO), B1 and E(TO +LO), A1(TO) and E(TO), A1(LO) and E(LO), respectively. The weak signal at $\sim 640\text{ cm}^{-1}$ (e) in the Raman spectrum of BT corresponds to a low amount of hexagonal phase, which might also be present in the materials due to in-plane residual stress [27].

The appearance of peak *a* upon Zr substitution is related to the Zr-O motion and indicates the successful incorporation of Zirconium in the material [28]. Upon increasing Zr content, peak broadening is visible, due to the increased translational disorder in the material. Already at 10 % of Zr substitution, the Raman modes appear much more diffuse in the recorded spectrum. Especially the change in peak *c*, which is the so-called ‘silent mode’ [29], is interesting, since this mode is an indicator of ferroelectric character. It seems, thus, that BZT thin films lose their macroscopic ferroelectric character (at room temperature) already at 10 % Zr content. In addition, the dip *a* at around 125 cm^{-1} , which is related to B-site cation ordering, might indicate the presence of Zr-rich regions, because it becomes more prominent with increased Zr content [30].

Since peak *f* is due the bending and stretching of the oxygen octahedra in the ferroelectric phase [31,32], the partial disappearance of it with increased Zr content is another indicator of the increased relaxor-like state in the material. Since mode *f* and other modes broaden but do not disappear, it can be concluded that the material is never entirely cubic at short-range even with 40 % Zr content [30].

The microstructure of the BZT thin films shown in Fig. 3, reveal dense layers with interconnected grains for all samples. It is noteworthy that, with increasing Zr substitution, the average grain size decreases, but also an apparent increase in porosity can be noticed from the SEM images. The grain size distribution (Fig. 4) narrows with increasing Zr content as well, which is in accordance with previous literature reports [33–36]. The larger ionic radius of Zr, compared to Ti, results in a higher energy barrier for the diffusion of Zr. Thus, grain growth, which is a result of diffusion processes, is more inhibited with higher Zr concentrations [33]. In general, the grain size is small for all compositions ($< 100\text{ nm}$), which is typical for BT-based materials; for example, in NaNbO_3 the grain size decreases with increasing BT content [37].

Large-area ($10 \times 10\ \mu\text{m}^2$) atomic force microscopy measurements (AFM) showed that all thin films obtained a smooth and homogenous surface. The AFM topography of the BT (see Fig. 5(a)), revealed regular

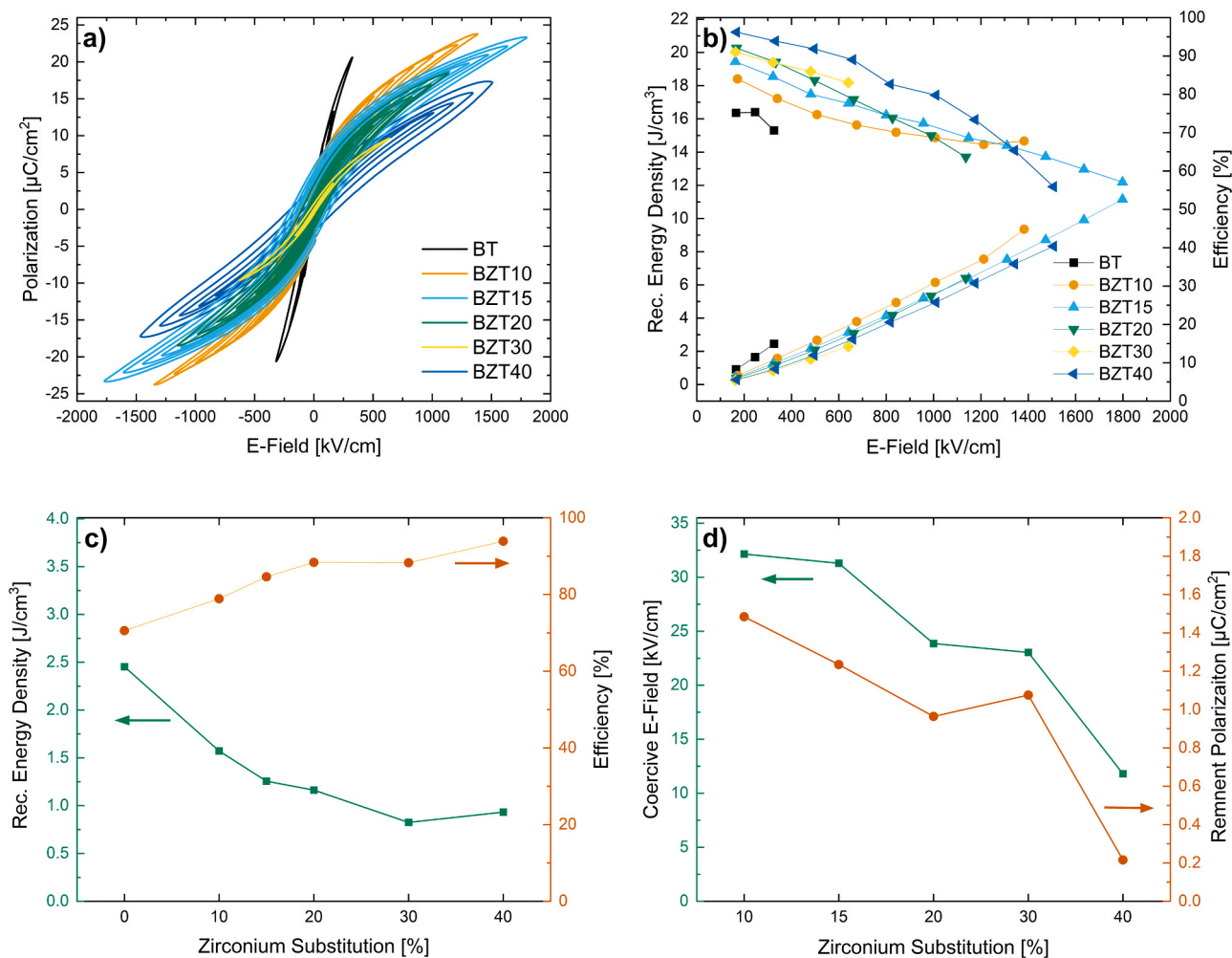


Fig. 6. Data obtained from P-E hysteresis measurements of BT, BZT10, BZT15, BZT20, BZT30 and BZT40 thin films at 1 kHz, room temperature and with dot2dot configuration (cf. Material and methods): (a) P-E hysteresis measurements up to the maximum electric field obtained for the different compositions, (b) calculated recoverable energy density and efficiency values for the different compositions and up to the maximum electric field, averaged values from 3 measurements, (c) calculated recoverable energy density and efficiency values for the different Zr substitutions at around 330 kVcm^{-1} , averaged values from 3 measurements, (d) coercive E-field values and remnant polarization values for the different Zr substitutions by applying up to $\sim 625\text{ kVcm}^{-1}$, averaged values from 3 measurements;

circular elevations in the submicron range, which is most likely due to the presence of columnar grains. With increasing Zr content, these elevations become less visible, the topography is less contrasted, probably due to the decreased grain size, which is consistent with the transition from a columnar to a finer-grained polycrystalline microstructure, as also indicated by SEM images (Fig. 3). However, at high Zr content (BZT30, BZT40) there are additional μm -sized defects (agglomerates, pits) in the topographies. The increasing number of defects is more apparent in the AFM micrographs, likely because of the larger measurement area ($10 \times 10\ \mu\text{m}^2$) compared to the smaller area in SEM images ($\sim 1 \times 1\ \mu\text{m}^2$), where the surfaces of BZT30 and BZT40 appear very smooth.

To further quantify the surface topography, roughness parameters were extracted from AFM data and are summarized in Table 1. The S_a (mean roughness) and S_q (root mean square roughness) values confirm that all films retain relatively low roughness, indicating a smooth surface morphology. However, a gradual increase in roughness is observed with increasing Zr content, particularly above 15 %, where larger surface irregularities such as voids and agglomerates become more pronounced. This trend correlates with the microstructural evolution observed in XRD and SEM analyses, further supporting the transition from a highly textured columnar growth to a more random polycrystalline arrangement.

3.2. Electrical characterization

The results obtained from the bipolar dynamic polarization-electric field (P-E) hysteresis loops measured at room temperature with a frequency of 1 kHz are presented in Fig. 6. Typical slim ferroelectric P-E hysteresis loops were measured for all compositions and energy storage values were derived from them (Fig. 6(b-d)). Despite using comparably large electrode areas (1 mm diameter) for each measured metal-insulator-metal (MIM) capacitor structure, which increases the likelihood of having critical defects in the measured area, slim P-E hysteresis loops were obtained for all compositions, signaling high efficiencies and high quality of the tested thin films. Moreover, the addition of 1.5 % Mn to the thin films helped to curb leakage currents. At low fields (330 kVcm^{-1} , Fig. 6c) a decrease in recoverable energy density with increasing Zr content was measured. The recoverable energy density of BZT30 is only 34 % of the value of BT, which signals a drastic decrease in saturation polarization. This might be related to the larger Zr ion, which cannot go off-center in the respective perovskite octahedral, and hence leads to the formation of non-polar regions in the lattice [8]. Moreover, these clusters (which are, effectively, non-polar Barium Zirconate clusters within a polar BT lattice) led to a breakdown of the long-range ferroelectric order, as well as decreasing grain sizes, as recorded in the SEM measurements [38]. Both the coercive field and remnant

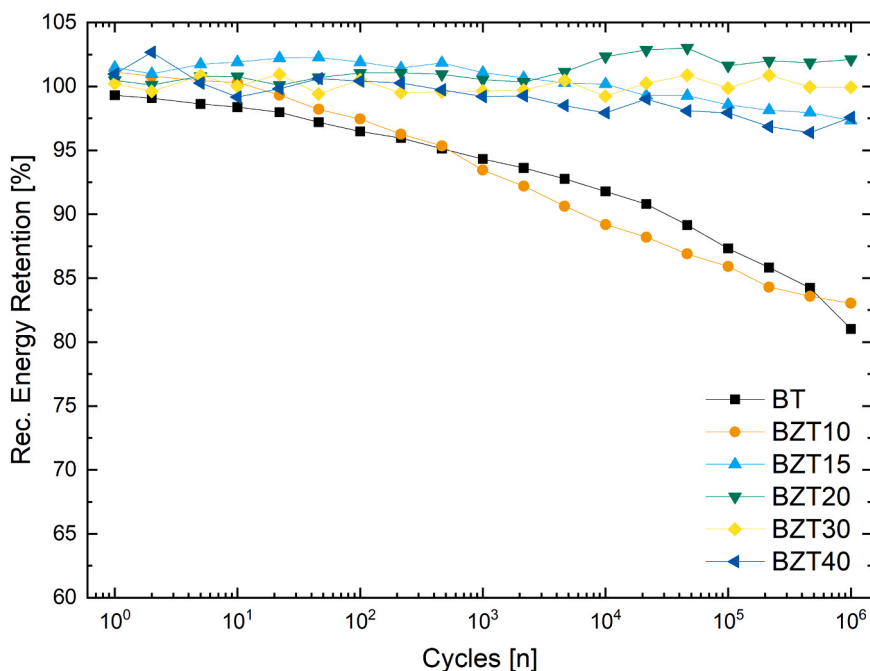


Fig. 7. Overview of the Recoverable energy retention ($W_{\text{rec}}/W_{\text{rec},0}$) of BT, BZT10, BZT15, BZT20, BZT30 and BZT40 thin films after unipolar dynamic cycling with 3 V (130 kVcm^{-1}), 1 kHz and with dot2dot configuration at room temperature.

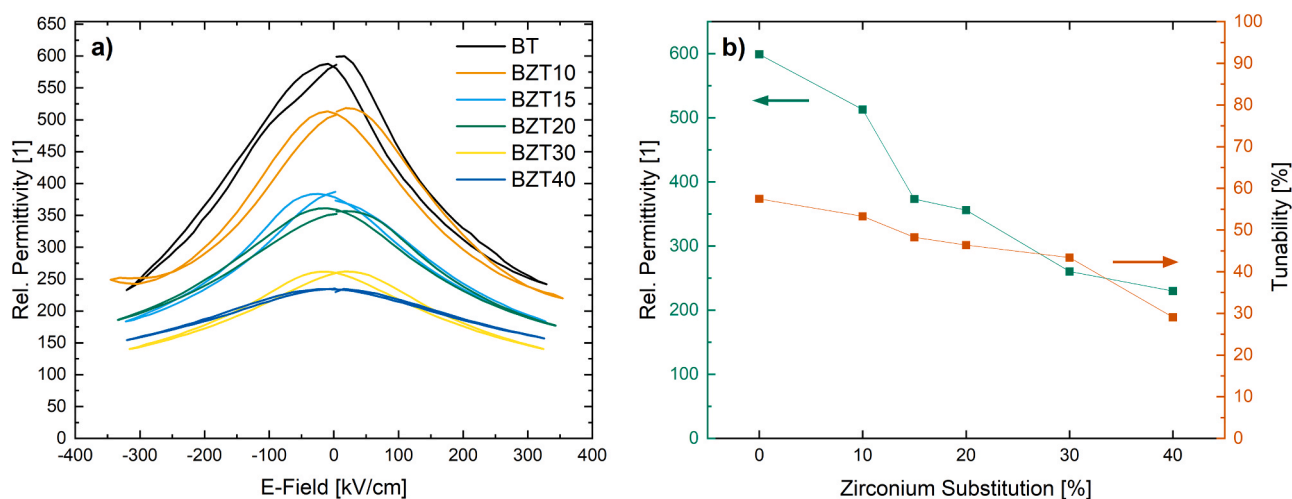


Fig. 8. Data obtained from Capacitance-Voltage measurements of BT, BZT10, BZT15, BZT20, BZT30 and BZT40 thin films at 1 kHz, room temperature and with dot2dot configuration: (a) Relative permittivity measured up to a specific E-field (300 kVcm^{-1}) (b) overview of the calculated relative permittivities and tunabilities.

polarization values decrease with increasing Zr content. Hence, the reversal of the polarization direction is facilitated with the increasing Zr substitution, which also explains the increased efficiency with increased Zr, which is in accordance with previous literature [39]. The BZT30 sample deviates from the observed trend, which is likely due to the increased amount of agglomerates on its surface measured by AFM (Fig. 5(e)), which could have led to irregular thickness in the area of electrodes. Since high efficiency is also obtained also for BT (75 %), low Zr substitution ($<30\%$) seems to be the most promising strategy to achieve high polarization output. BZT15, for instance, can withstand much higher electric fields ($\sim 1800 \text{ kVcm}^{-1}$) than pure BT, which fails at around 350 kVcm^{-1} (cf. Fig. 6b). As a result, with 15 % zirconium, the highest recoverable energy density of approximately $\sim 11 \text{ Jcm}^{-3}$ was achieved under an electric field of about 1800 kVcm^{-1} . The onset of relaxor-like behavior can be inferred from the P-E hysteresis loops to be around 10 % Zr, which is consistent with the indications from Raman

and XRD. The values reported on the graphs are the average out of three measurements that were carried out on the same MIM capacitor structure. The variation of the measured values within those three measurements remained always well below 10 %. We chose not to draw error bars on the diagrams because data collected on a much larger amount of samples would be necessary for a thorough statistical analysis. This exceeds the scope of our work.

The electrical fatigue behavior in the BZT films (Fig. 7) was investigated by unipolar dynamic cycling at room temperature with a frequency of 1 kHz and a 130 kVcm^{-1} bias. All compositions have a high retention of the recoverable energy density ($>80\%$), and for Zr substitution in the range $x = 0.15\text{--}0.40$, there is no significant decrease in recoverable energy density over the 10^6 applied loops. This further shows that 15 % Zr substitution seems to be the optimal composition for energy storage applications, by combining the highest recoverable energy (cf. Fig. 6) with excellent electrical fatigue behavior (cf. Fig. 7).

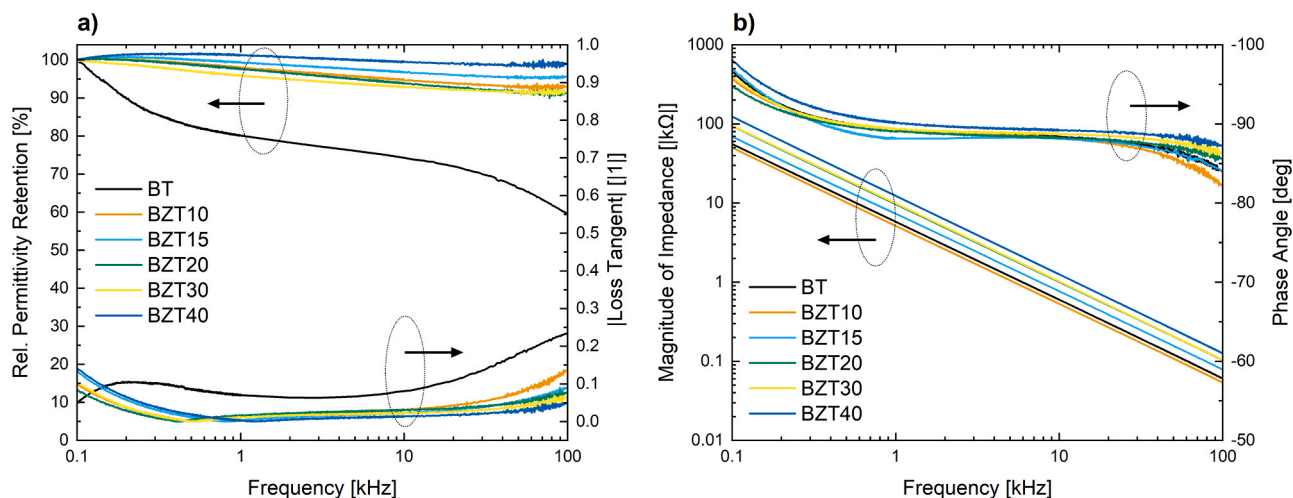


Fig. 9. Data obtained from Impedance measurements from 0.1 to 100 kHz of BT, BZT10, BZT15, BZT20, BZT30 and BZT40 thin films at room temperature and with bottom2dot configuration: (a) Retention of the relative permittivity ($\epsilon_r/\epsilon_{r,0}$) and magnitude of loss tangent for the different compositions, (b) Bode plot showing magnitude of impedance and the phase angle for the different compositions;

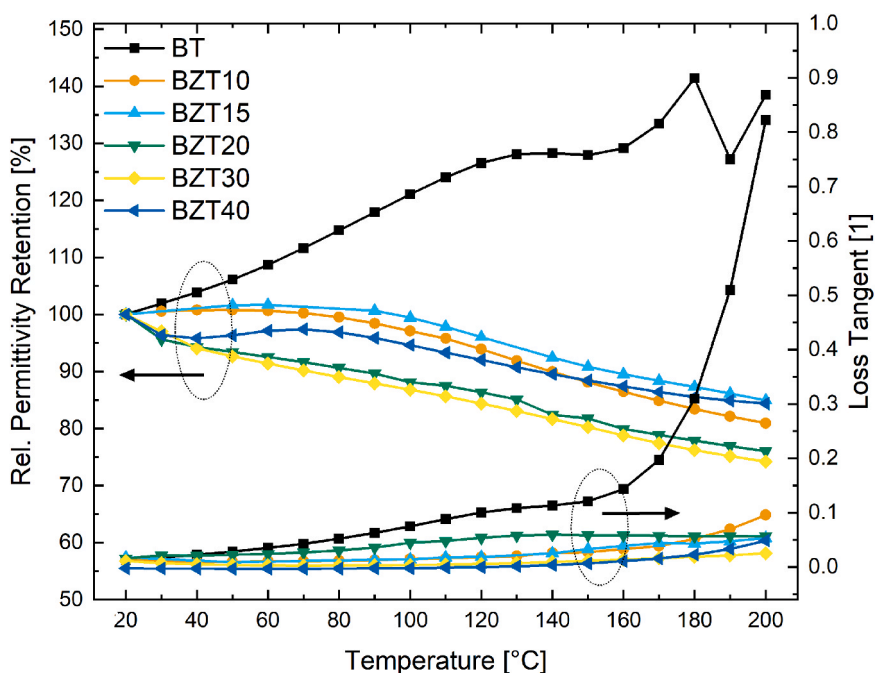


Fig. 10. Retention of Relative Permittivity ($\epsilon_r/\epsilon_{r,0}$) and Loss Tangent obtained from Impedance measurements of BT, BZT10, BZT15, BZT20, BZT30 and BZT40 thin films at different temperatures (20–200 °C) and 1 kHz with bottom2dot configuration.

The Capacitance-Voltage (C-V) measurements (Fig. 8) exhibit the same trends as the P-E hysteresis loops. A very high relative permittivity of ~ 600 is reached for BT at room temperature and 1 kHz, which is well above the values reported in the literature for sol-gel derived BT thin films [40,41]. This high value is remarkable considering the low thickness of our thin films (~ 150 nm), since the permittivity typically decreases with reduced thickness [42]. This shows that our proposed aqueous CSD leads to high quality thin films, which obtain competitive electric responses. The decrease of the relative permittivity down to ~ 230 (BZT40) with increasing Zr content is most likely a result of the decrease in grain size [38], and the introduction of the aforementioned non-polar clusters. Therefore, to maintain high permittivity values, high Zr substitution ($>20\%$) should be avoided. The tunability at 300 kVcm^{-1} is also lowered with increasing Zr content (BT: 58 %, BZT40: 29 %), which is expected, as tunability is typically proportional to the

permittivity of a sample [43]. Hence, the tunability can be tailored with the Zr content and for applications where high permittivity and tunability is required, like microwave tunable applications, Zr contents below 10 % are most suitable.

Results obtained from impedance measurements are displayed in Fig. 9. The relative permittivity is stable over a broad frequency range (100 Hz-100 kHz) for Zr-substituted compositions, with less than 12 % decrease from the value at 100 Hz. However, for BT there is a significant immediate decrease in relative permittivity with rising frequency and at 100 kHz the relative permittivity is less than 60 % of the value at 100 Hz. Hence, Zr substitution stabilizes the permittivity of the BZT thin films over a wide frequency range. The highest substitution (40 %) leads to the lowest deviation ($<3\%$) from the value measured at 100 Hz, likely due to the increasing concentration of dynamic nanodomains. Consequently, for applications like memristors or Dynamic Random

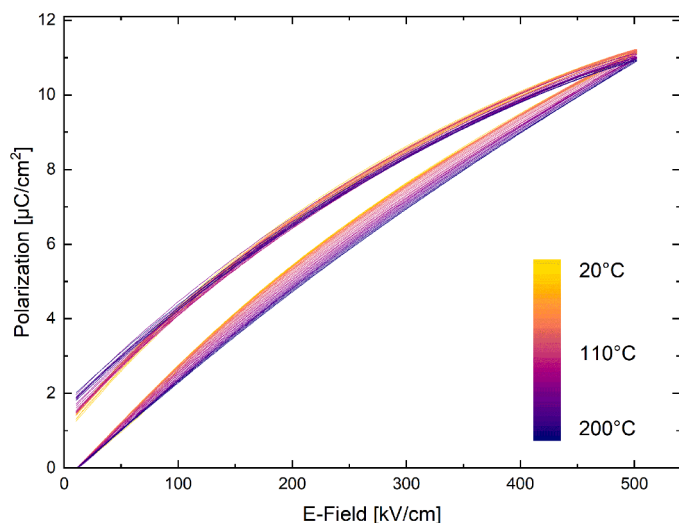


Fig. 11. Unipolar dynamic P-E hysteresis measurements of BZT15 thin films obtained at different temperatures and 1 kHz with bottom2dot configuration.

Access Memories (DRAM), which require high frequency, high Zr substitution is advantageous. Moreover, the loss tangent remains low for the Zr-substituted compositions in all frequency ranges due to the high efficiency of the thin films. Noticeably higher tangent losses were measured for BT, in comparison to the Zr-substituted compositions.

Higher impedance was reached with increasing Zr substitution and a maximum impedance of over 100 k Ω was achieved with 40 % substitution. This could have been caused by varying grain sizes for the different compositions, since grain boundaries lead to slower electron transport (increased electrical resistance). The impedance decreases according to a power function for all compositions, seen by the linear trend in the double-logarithmic plot. The phase angle remains around -90° for all compositions and frequencies, due to the capacitive resistance. However, at high frequencies (>10 kHz) and low frequencies (<1 kHz) the phase angle deviates slightly from the -90° , which signals that at these frequencies there is stronger resistive contributions.

With increased Zirconium substitution in BZT, the temperature of the relative permittivity maxima (T_m) at the paraelectric to ferroelectric phase-transition is typically shifted to lower temperature and the relative permittivity peaks at the phase-transitions become more diffuse [44]. According to literature on BZT single crystals, the T_m can be

expected to be around 120 $^\circ\text{C}$ for BT, 80 $^\circ\text{C}$ for BZT10, 70 $^\circ\text{C}$ for BZT15, 35 $^\circ\text{C}$ for BZT20 and -50 $^\circ\text{C}$ for BZT30 [45]. The effects of the temperature on the permittivity, loss tangent and polarization on the prepared BZT thin films are illustrated in Fig. 10. No clear T_m can be derived from our measurements; however, diffuse maxima can be identified for BZT10 and BZT15 between 20 $^\circ\text{C}$ and 70 $^\circ\text{C}$. For higher substituted compositions, the relative permittivity maxima are likely below the measured range (20–200 $^\circ\text{C}$). For BT, there is a broad maximum around 140 $^\circ\text{C}$, and at higher temperatures the polarization values seem to be distorted due to the influence of the rising losses. In general, the relative permittivity vs. temperature curves seem to be rather flat: the maxima are hard to distinguish, and at slightly higher values than what is expected according to literature. This early onset of diffuseness and “relaxor-like” behavior, indicated by the strong difference in the retention in the relative permittivity of BT and BZT10, may be attributed to microstructural influences. Not just reduced grain size was indicated by SEM but also GIXRD analysis reveals a clear peak broadening of the {110}, indicating reduction in crystallite size. This microstructural refinement leads to a higher density of grain boundaries, which might act as interfaces disrupting long-range ferroelectric order [13]. The reduced grain size thus appears to play a significant role in triggering early relaxor-like characteristics, even before reaching the Zr content typically required for a full transition from ferroelectric to relaxor ferroelectric behavior.

The early onset of relaxor-like behavior may also be triggered by the possible presence of low-dielectric permittivity interface layers (‘dead layer’), which could have originated from the repeated thermal annealing of the thin films on the Pt/Si substrates at 850 $^\circ\text{C}$. These interfacial layers might induce internal electric field fluctuations and impede domain wall motion, thereby promoting relaxor-like behavior at low Zr content [46]. This effect may be particularly significant in our case due to the relatively low thickness of the films (~ 150 nm) [47].

Overall, the Zr substitution leads to very high temperature stability, which makes the thin films meet the temperature specifications for R capacitors (± 15 %) [48] up to a maximum temperature of 160 $^\circ\text{C}$ for BZT10, 190 $^\circ\text{C}$ for BZT15, 130 $^\circ\text{C}$ for BZT20, 110 $^\circ\text{C}$ for BZT30 and 180 $^\circ\text{C}$ for BZT40. This is a drastic increase in the temperature range, compared to pure BT, which would deviate more than 15 % in permittivity above 80 $^\circ\text{C}$. Moreover, the loss tangent remains very low and stable (<0.1) for the whole measured temperature range (20–200 $^\circ\text{C}$) of the BZT thin films, further establishing the high-quality and temperature stability of the films. However, for pure BT, there is a sharp rise in the loss tangent above 150 $^\circ\text{C}$, meaning there might be thermally activated conduction

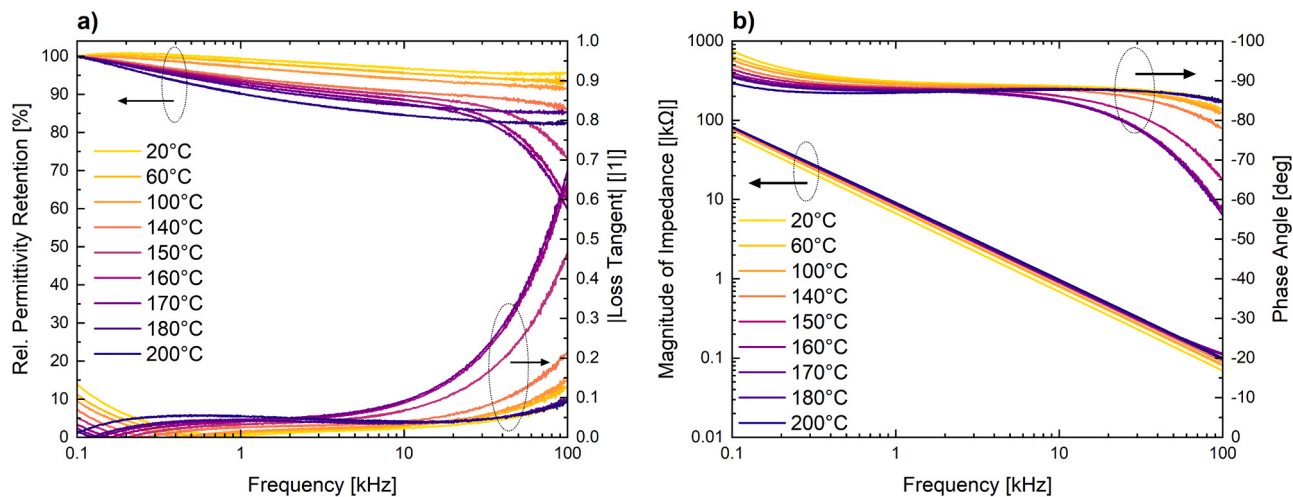


Fig. 12. Data obtained from Impedance measurements of BZT15 thin films from 0.1 to 100 kHz at different temperatures (20–200 $^\circ\text{C}$) and with bottom2dot configuration: (a) Retention of the relative permittivity ($\epsilon_r/\epsilon_{r,0}$) and magnitude of loss tangent for the different temperatures, (b) Bode plot showing magnitude of impedance and the phase angle for the different temperatures;

losses present in BT in the vicinity of to the expected Curie temperature.

In Fig. 11 the change of the unipolar dynamic P-E hysteresis with temperature is shown for the best-performing composition: BZT15. Minor changes in the polarization are observed for the measured temperature range (20–200°C), namely a decrease of 2.7 % in the maximum polarization and a 24.1 % increase in remnant polarization with increasing temperature. This is in good agreement with the relative permittivity retention values for BZT15 acquired from the impedance measurements (cf. Fig. 10).

In Fig. 12 the dependence of the permittivity, loss tangent, impedance and phase angle of the best-performing composition BZT15 with respect to frequency and temperature is depicted. For all temperatures (20–200°C), the permittivity of BZT15 decreases with rising frequency; this frequency dispersion of permittivity is a typical property of relaxor systems [49], which suggests that relaxor behavior is attained in our BZT thin films at 15 % Zr content. High-frequency stability (<9 %) is obtained in BZT15 for temperatures below 150°C and a frequency range of 0.1 – 100 kHz. For low temperature applications, the highest permittivity values can be achieved at an operating frequency of around 200 Hz. The loss tangent remains low for most temperatures (<0.2, 20–200°C) over the measured frequency range (0.1 – 100 kHz). However, from 150°C to 170°C there is a distinct increase in the loss tangent at frequencies above 5 kHz and a strong reduction in relative permittivity above 20 kHz was measured. Hence, at this temperature range and with increasing frequency there are significant losses occurring in BZT15, which could indicate the appearance of temperature-dependent charge-carriers induced by fast switching in the material.

Interestingly, with increasing temperature, higher impedance is also achieved for BZT15. The impedance decreases for all temperatures with increasing frequency following a power function. The phase angle remains around -90° for all temperatures and frequencies, due to the dominating capacitive resistance. However, from 150°C to 170°C and at frequencies above 5 kHz, the phase angle deviates distinctively from the -90° , which could mean that at these frequencies and this temperature range there is stronger resistive contributions. Also at frequencies below 3 kHz a shift in the phase angle was measured, which is more pronounced at lower temperatures, signaling again an increased share of resistive contributions under these conditions.

In summary, $\text{BaZr}_x\text{Ti}_{1-x}\text{O}_3$ (BZT) thin films were fabricated by a novel, environmentally friendly aqueous CSD process in the compositional range $x = 0-0.40$. Structural investigation with XRD and Raman spectroscopy showed that the thin films were phase pure with a tetragonal perovskite structure, whereby the onset of relaxor-like behavior occurred already at 10 % Zr substitution. All thin films had dense microstructure with submicron interconnected grains as demonstrated by SEM and AFM analyses, whereby the grain sizes decreased with increasing Zr content due to the Zr-induced increased energy barrier for ionic diffusion. Electrical characterization showed that any level of Zr substitution significantly improved the performance of the thin films. High energy storage efficiencies and long-term retention of recoverable energy density over a wide frequency range were obtained for all the BZT films, signaling their high quality. Further, impedance measurements showed low loss tangents and improved temperature stability for Zr-substituted films. The highest electrical fields were applicable in films with 15 % Zr substitution, leading to the highest recoverable energy density of $\sim 11 \text{ J cm}^{-3}$. This composition displayed excellent electrical fatigue behavior and high thermal stability up to 200 °C, making it optimal for energy storage applications such as multilayer ceramic capacitors. Hence, we are convinced that our optimized, novel and environmentally friendly aqueous CSD process is suitable for the production of high-quality and reliable thin films for energy storage capacitors especially for IoT applications. The electrical results are in good agreement with values from Luo *et al.*, who also reported high temperature, frequency and fatigue stability for their $\text{BaZr}_{0.2}\text{Ti}_{0.8}\text{O}_3-0.02 \text{ MnO}_2$ thin films, which however, were prepared using 2-methoxyethanol [50].

4. Conclusions

Dense, phase pure $\text{BaZr}_x\text{Ti}_{1-x}\text{O}_3$ (BZT) thin films on Pt/Si substrates were fabricated with a novel aqueous chemical solution deposition (CSD) process. A wide compositional range was investigated ($x = 0-0.40$) and structural characterization showed that relaxor-like behavior was induced already with 10 % Zr substitution. The room temperature P-E hysteresis loops, electrical fatigue behavior and temperature stability were investigated and confirmed the high performance of the BZT films obtained from aqueous CSD. The electrical response of the BZT thin films depends strongly on the Zr substitution level and can be tailored depending on the application, but for energy storage purposes, we highlight the composition with 15 % Zr content as the most promising.

CRedit authorship contribution statement

Deluca Marco: Writing – review & editing, Supervision, Funding acquisition. **Angermann Martina:** Writing – review & editing, Writing – original draft, Visualization, Investigation, Formal analysis, Data curation, Conceptualization. **Panzic Ivana:** Writing – review & editing, Supervision, Investigation. **Gindel Theresa:** Writing – review & editing, Investigation. **Bakken Kristine:** Writing – review & editing, Supervision, Investigation, Conceptualization. **Kobald Alexander:** Writing – review & editing, Software. **Kobald Herbert:** Writing – review & editing, Software.

Funding sources

This work was supported by the European Union's Horizon 2020 Research and Innovation Programme under grant agreement Nr. 951774 and the European Research Council (ERC) under the European Union's Horizon 2020 research and innovation programme (grant agreement No. 817190). The authors gratefully acknowledge the financial support under the scope of the COMET program within the K2 Center "Integrated Computational Material, Process and Product Engineering (IC-MPPE)" (Project No 886385). This program is supported by the Austrian Federal Ministries for Climate Action, Environment, Energy, Mobility, Innovation and Technology (BMK) and for Labour and Economy (BMAW), represented by the Austrian Research Promotion Agency (FFG), and the federal states of Styria, Upper Austria and Tyrol.

Declaration of Competing Interest

The authors declare that they have no known competing financial interests or personal relationships that could have appeared to influence the work reported in this paper.

Acknowledgements

The authors acknowledge the technical assistance for the SEM measurements from Julian Wagner and Bernhard Sartory.

References

- [1] G.R. Love, Energy storage in ceramic dielectrics, *J. Am. Ceram. Soc.* 73 (2) (1990) 323–328, <https://doi.org/10.1111/J.1151-2916.1990.TB06513.X>.
- [2] P. Zhao, et al., High-performance relaxor ferroelectric materials for energy storage applications, *Adv. Energy Mater.* 9 (17) (May 2019), <https://doi.org/10.1002/AENM.201803048>.
- [3] X.K. Wei, N. Domingo, Y. Sun, N. Balke, R.E. Dunin-Borkowski, J. Mayer, Progress on emerging ferroelectric materials for energy harvesting, storage and conversion, *Adv. Energy Mater.* 12 (24) (Jun. 2022) 2201199, <https://doi.org/10.1002/AENM.202201199>.
- [4] Y. Huang, C. Zhao, B. Wu, J. Wu, Multifunctional BaTiO_3 -based relaxor ferroelectrics toward excellent energy storage performance and electrostrictive strain benefiting from crossover region, *ACS Appl. Mater. Interfaces* 12 (21) (May 2020) 23885–23895, <https://doi.org/10.1021/acsami.0c03677>.

- [5] V. Veerapandiyam, F. Benes, T. Gindl, M. Deluca, Strategies to improve the energy storage properties of perovskite lead-free relaxor ferroelectrics: a review, *Materials* 13 (24) (Dec. 2020) 5742, <https://doi.org/10.3390/ma13245742>.
- [6] T. Maiti, R. Guo, A.S. Bhalla, Evaluation of experimental resume of BaZr_xTi_{1-x}O₃ with perspective to ferroelectric relaxor family: an overview, *Ferroelectrics* 425 (1) (Jan. 2011) 4–26, <https://doi.org/10.1080/00150193.2011.644168>.
- [7] M. Usman, A. Mumtaz, S. Raoof, S.K. Hasanain, Order parameter and scaling behavior in BaZr_xTi_{1-x}O₃ (0.3 < x < 0.6) relaxor ferroelectrics, *Appl. Phys. Lett.* 103 (Dec. 2013) 26, <https://doi.org/10.1063/1.4860967>.
- [8] W. Kleemann, Random fields in relaxor ferroelectrics — a jubilee review, *J. Adv. Dielectr.* 02 (02) (Apr. 2012) 1241001, <https://doi.org/10.1142/S2010135X12410019>.
- [9] O. Aktas, et al., Phase transition and polar cluster behavior above Curie temperature in ferroelectric BaTi_{0.8}Zr_{0.2}O₃, *Appl. Phys. Lett.* 124 (19) (May 2024), <https://doi.org/10.1063/5.0195017>.
- [10] A. Tachafine, et al., Classical and relaxor ferroelectric behavior of titanate of barium and zirconium ceramics, *Spectrosc. Lett.* 47 (5) (May 2014) 404–410, <https://doi.org/10.1080/00387010.2013.872664>.
- [11] A. Simon, J. Ravez, M. Maglione, The crossover from a ferroelectric to a relaxor state in lead-free solid solutions, *J. Phys. Condens. Matter* 16 (6) (Feb. 2004) 963–970, <https://doi.org/10.1088/0953-8984/16/6/023>.
- [12] N. Binhayeeniyi, P. Sukwisute, S. Nawae, N. Muensit, Energy conversion capacity of barium zirconate titanate, *Materials* 13 (2) (Jan. 2020) 315, <https://doi.org/10.3390/ma13020315>.
- [13] T. Hoshina, T. Furuta, T. Yamazaki, H. Takeda, T. Tsurumi, Grain size effect on dielectric properties of Ba(Zr,Ti)₂O₇ Ceramics, *Jpn. J. Appl. Phys.* 51 (9S1) (Sep. 2012) 09LC04, <https://doi.org/10.1143/JJAP.51.09LC04>.
- [14] Z. Sun, et al., Superior capacitive energy-storage performance in Pb-free relaxors with a simple chemical composition, *J. Am. Chem. Soc.* 145 (11) (Mar. 2023) 6194–6202, <https://doi.org/10.1021/jacs.2c12200>.
- [15] A.R. Jayakrishnan, et al., Are lead-free relaxor ferroelectric materials the most promising candidates for energy storage capacitors? *Prog. Mater. Sci.* 132 (Feb. 2023) 101046 <https://doi.org/10.1016/j.pmatsci.2022.101046>.
- [16] G. Hu, et al., Improved leakage behavior at high temperature via engineering of ferroelectric sandwich structures, *Materials* 16 (2) (Jan. 2023) 712, <https://doi.org/10.3390/ma16020712>.
- [17] T.M. Raeder, K. Bakken, J. Glau, M.A. Einarsrud, T. Grande, Enhanced in-plane ferroelectricity in BaTiO₃ thin films fabricated by aqueous chemical solution deposition, *AIP Adv.* 8 (10) (Oct. 2018) 2–11, <https://doi.org/10.1063/1.5059549>.
- [18] K. Bakken, et al., Tailoring preferential orientation in BaTiO₃-based thin films from aqueous chemical solution deposition, *Chem. Methods* 2 (2) (Feb. 2022), <https://doi.org/10.1002/cmtd.202100064>.
- [19] A. Hardy, et al., Crystallization resistance of barium titanate zirconate ultrathin films from aqueous CSD: a study of cause and effect, *J. Mater. Chem.* 19 (8) (2009) 1115, <https://doi.org/10.1039/b816856c>.
- [20] A. Berksoy-Yavuz, E. Mensur-Alkoy, E. Erdem, S. Alkoy, Electrical properties, EPR analyses and defect chemistry of Mn-doped 0.675PMN-0.325PT piezoceramics, *Ceram. Int.* 46 (18) (Dec. 2020) 28980–28986, <https://doi.org/10.1016/j.ceramint.2020.08.069>.
- [21] E. Khomyakova, et al., On the formation mechanism of Ba_{0.85}Ca_{0.15}Zr_{0.1}Ti_{0.9}O₃ thin films by aqueous chemical solution deposition, *J. Eur. Ceram. Soc.* 40 (15) (Dec. 2020) 5376–5383, <https://doi.org/10.1016/j.jeurceramsoc.2020.07.042>.
- [22] D. Necas, P. Klapeček, Gwyddion: an open-source software for SPM data analysis, *Open Phys.* 10 (1) (Jan. 2012), <https://doi.org/10.2478/s11534-011-0096-2>.
- [23] I. Burn, D. Smyth, Energy storage in ceramic, *J. Mater. Sci.* 7 (1972) 339–343.
- [24] H. Lee, S. Moon, C. Choi, D.K. Kim, Synthesis and size control of tetragonal barium titanate nanopowders by facile solvothermal method, *J. Am. Ceram. Soc.* 95 (8) (Aug. 2012) 2429–2434, <https://doi.org/10.1111/j.1551-2916.2012.05085.x>.
- [25] P.S. Aktaş, Structural investigation of barium zirconium titanate Ba(Zr_{0.5}Ti_{0.5})O₃ particles synthesized by high energy ball milling process, *J. Chem. Sci.* 132 (1) (Dec. 2020) 130, <https://doi.org/10.1007/s12039-020-01837-7>.
- [26] S. Mahajan, O.P. Thakur, K. Prakash, K. Sreenivas, Effect of Zr on dielectric, ferroelectric and impedance properties of BaTiO₃ ceramic, *Bull. Mater. Sci.* 34 (7) (Dec. 2011) 1483–1489, <https://doi.org/10.1007/s12034-011-0347-2>.
- [27] K. Tsuzuku, M. Couzi, In situ investigation of chemical reactions between BaCO₃ and anatase or rutile TiO₂, *J. Mater. Sci.* 47 (10) (May 2012) 4481–4487, <https://doi.org/10.1007/s10853-012-6310-9>.
- [28] J. Kreisel, P. Bouvier, M. Maglione, B. Dkhil, A. Simon, High-pressure Raman investigation of the Pb-free relaxor BaTi_{0.65}Zr_{0.35}O₃, *Phys. Rev. B* 69 (9) (Mar. 2004) 092104, <https://doi.org/10.1103/PhysRevB.69.092104>.
- [29] G. Burns, Lattice modes in ferroelectric perovskites. II. Pb_{1-x}Ba_xTiO₃ including BaTiO₃, *Phys. Rev. B* 10 (5) (Sep. 1974) 1951–1959, <https://doi.org/10.1103/PhysRevB.10.1951>.
- [30] V. Buscaglia, et al., Average and local atomic-scale structure in BaZr_xTi_{1-x}O₃ (x = 0.10, 0.20, 0.40) ceramics by high-energy x-ray diffraction and Raman spectroscopy, *J. Phys. Condens. Matter* 26 (6) (Feb. 2014) 065901, <https://doi.org/10.1088/0953-8984/26/6/065901>.
- [31] A. Feteira, D.C. Sinclair, J. Kreisel, Average and local structure of (1-x)BaTiO₃-xLaYO₃ (0 ≤ x ≤ 0.50) Ceramics, *J. Am. Ceram. Soc.* 93 (12) (Dec. 2010) 4174–4181, <https://doi.org/10.1111/j.1551-2916.2010.04006.x>.
- [32] A. Gajović, J.V. Plešćina, K. Zagar, M. Plodinec, S. Šturm, M. Čeh, Temperature-dependent Raman spectroscopy of BaTiO₃ nanorods synthesized by using a template-assisted sol-gel procedure, *J. Raman Spectrosc.* 44 (3) (Mar. 2013) 412–420, <https://doi.org/10.1002/jrs.4206>.
- [33] C. Gao, J. Zhai, X. Yao, Preparation and dielectric properties of Ba(Zr_xTi_{1-x})O₃ thin films grown by a sol-gel process, *Integr. Ferroelectr.* 74 (1) (Sep. 2005) 147–153, <https://doi.org/10.1080/10584580500414119>.
- [34] J. Zhai, D. Hu, X. Yao, Z. Xu, H. Chen, Preparation and tunability properties of Ba(Zr_xTi_{1-x})O₃ thin films grown by a sol-gel process, *J. Eur. Ceram. Soc.* 26 (10–11) (Jan. 2006) 1917–1920, <https://doi.org/10.1016/j.jeurceramsoc.2005.09.021>.
- [35] L. Xu, Y. Xu, Effect of Zr⁴⁺ content on crystal structure, micromorphology, ferroelectric and dielectric properties of Ba(Zr_xTi_{1-x})O₃ ceramics, *J. Mater. Sci. Mater. Electron* 31 (7) (Apr. 2020) 5492–5498, <https://doi.org/10.1007/s10854-020-03114-2>.
- [36] J. Zhai, X. Yao, J. Shen, L. Zhang, H. Chen, Structural and dielectric properties of Ba(Zr_xTi_{1-x})O₃ thin films prepared by the sol-gel process, *J. Phys. D: Appl. Phys.* 37 (5) (Mar. 2004) 748–752, <https://doi.org/10.1088/0022-3727/37/5/016>.
- [37] A.M. Kobald, H. Kobald, M. Deluca, Phase stability and energy storage properties of polycrystalline antiferroelectric BaTiO₃-substituted NaNbO₃ thin films, *J. Eur. Ceram. Soc.* 44 (5) (May 2024) 2831–2841, <https://doi.org/10.1016/j.jeurceramsoc.2023.11.071>.
- [38] C. Fu, H. Chen, L. Hu, W. Cai, C. Yang, Model for grain size effect on dielectric nonlinearity of ferroelectrics, *Integr. Ferroelectr.* 92 (1) (Dec. 2007) 114–122, <https://doi.org/10.1080/10584580701748513>.
- [39] H. Chen, C. Yang, C. Fu, J. Shi, J. Zhang, W. Leng, Microstructure and dielectric properties of BaZr_xTi_{1-x}O₃ ceramics, *J. Mater. Sci. Mater. Electron* 19 (4) (Apr. 2008) 379–382, <https://doi.org/10.1007/s10854-007-9348-8>.
- [40] H.B. Sharma, Structure and properties of BT and BST thin films, *Ferroelectrics* 453 (1) (Jan. 2013) 113–121, <https://doi.org/10.1080/00150193.2013.842139>.
- [41] S. Song, J. Zhai, X. Yao, Effects of buffer layer on the dielectric properties of BaTiO₃ thin films prepared by sol-gel processing, *Mater. Sci. Eng. B* 145 (1–3) (Dec. 2007) 28–33, <https://doi.org/10.1016/j.mseb.2007.09.045>.
- [42] C.B. Parker, J.-P. Maria, A.I. Kingon, Temperature and thickness dependent permittivity of (Ba,Sr)TiO₃ thin films, *Appl. Phys. Lett.* 81 (2) (Jul. 2002) 340–342, <https://doi.org/10.1063/1.1490148>.
- [43] A. Outzourhit, J.U. Trefny, T. Kito, B. Yarar, A. Nazirpour, A.M. Hermann, Fabrication and characterization of Ba_{1-x}Sr_xTiO₃ tunable thin film capacitors, *Thin Solid Films* 259 (2) (Apr. 1995) 218–224, [https://doi.org/10.1016/0040-6090\(94\)06451-2](https://doi.org/10.1016/0040-6090(94)06451-2).
- [44] T. Maiti, R. Guo, A.S. Bhalla, Structure-property phase diagram of BaZr_xTi_{1-x}O₃ system, *J. Am. Ceram. Soc.* 91 (6) (Jun. 2008) 1769–1780, <https://doi.org/10.1111/j.1551-2916.2008.02442.x>.
- [45] J. Peng, et al., A thermodynamic potential for barium zirconate titanate solid solutions, *npj Comput. Mater.* 4 (1) (Nov. 2018) 66, <https://doi.org/10.1038/s41524-018-0126-3>.
- [46] M. Stengel, N.A. Spaldin, Origin of the dielectric dead layer in nanoscale capacitors, *Nature* 443 (7112) (Oct. 2006) 679–682, <https://doi.org/10.1038/nature05148>.
- [47] C. Basceri, S.K. Streiffer, A.I. Kingon, R. Waser, The dielectric response as a function of temperature and film thickness of fiber-textured (Ba,Sr)TiO₃ thin films grown by chemical vapor deposition, *J. Appl. Phys.* 82 (5) (Sep. 1997) 2497–2504, <https://doi.org/10.1063/1.366062>.
- [48] TDK, Temperature characteristics guide (3): Which Temperature Characteristic are commonly referenced for MLCCs (Multilayer Ceramic Chip Capacitors)? 2024. (<https://product.tdk.com/en/contact/faq/capacitors-0051.html>).
- [49] S. Sidorkin, et al., Dispersion of dielectric permittivity in thin ferroelectric lead titanate films, *Solid State Phenom.* 115 (Aug. 2006) 233–238, <https://doi.org/10.4028/www.scientific.net/SSP.115.233>.
- [50] Y. Luo, G. Qiu, J. Wang, Y. Liu, J. Luo, Y. Lyu, Optimization of energy-storage performance of Mn-doped BaZr_{0.2}Ti_{0.8}O₃ lead-free ferroelectric thin films by the sol-gel method, *J. Sol. Gel Sci. Technol.* 107 (3) (Sep. 2023) 560–568, <https://doi.org/10.1007/s10971-023-06150-6>.